The role of texturing and microstructure evolution on the tensile behavior of heat-treated Inconel 625 produced via laser powder bed fusion

The role of texturing and microstructure evolution on the tensile behavior of heat-treated Inconel 625 produced via laser powder bed fusion

Giulio Marchese[1,*], Simone Parizia[1,2], Masoud Rashidi[3], Abdollah Saboori[1], Diego Manfredi[2], Daniele Ugues[1], Mariangela Lombardi[1], Eduard Hryha[3], Sara Biamino[1]

[1]*Department of Applied Science and Technology, Politecnico di Torino, Corso Duca degli Abruzzi 24, 10129 Torino, Italy*

[2]*Center for Sustainable Future Technologies - CSFT@PoliTo, Istituto Italiano di Tecnologia, Via Livorno 60, 10144 Torino, Italy*

[3]*Department of Industrial and Materials Science, Chalmers University of Technology, 41296 Göteborg, Sweden*

Abstract

Inconel 625 (IN625) alloy has high-temperature strength coupled with high oxidation and corrosion resistance. Additionally, due to its excellent weldability, IN625 can be processed by laser powder bed fusion (LPBF) additive manufacturing (AM) process allowing the production of complex shapes. However, post-AM heat treatment is necessary to develop the desired microstructure and mechanical properties to meet industrial needs. This work is focused on the influence of different heat treatment processes, namely stress relieving, recrystallization annealing and solution annealing on the microstructure and tensile properties of LPBF IN625 alloy. Investigation of the crystallographic texture by electron backscattered diffraction indicated that heat treatments at 1080 °C and 1150 °C tend to eliminate anisotropy in the material by the recrystallization and grain growth resulting in the formation of equiaxed grains. Tensile properties of heat-treated LPBF IN625 alloy built along different orientations revealed higher tensile properties than the minimum recommended values of wrought IN625 alloy in the annealed and solution annealed states.

Keywords: Laser powder bed fusion (LPBF); Inconel 625 (IN625); texture; microstructure; electron backscattered diffraction (EBSD); tensile properties.

1.0 Introduction

Nowadays, laser powder bed fusion (LPBF) process represents one of the predominant additive manufacturing techniques for the production of Ni-based superalloys [1–3]. The LPBF process allows the fabrication of components through the addition of material layer by layer, giving the possibility to generate very complex shape parts in contrast to traditional manufacturing methods such as subtractive or joining techniques [2–4]. This potentiality drives the interest in the development and production of Ni-based superalloys by LPBF, especially when complex shapes are required. This is also more attractive considering that these alloys are typically difficult to machining due to their high hardness [5,6]. However, some Ni-based superalloys can be subjected to the crack formation under LPBF process, as reported for Hastelloy X and CM247LC [7–10].

Among the crack-free LPBF Ni-based superalloys, on the other hand, Inconel 625 (IN625) presents a combination of high-temperature strength and very high corrosion and oxidation resistance [11,12]. Due to its properties, this alloy has been widely used for application in harsh conditions from cryogenic temperature up to around 980 °C [12,13]. At the current state-of-the-art, the established and commercialized process parameters for LPBF allows to produce defect-free components of IN625 with a density close to 100 % thanks to its high weldability [8,14,15]. However, LPBF IN625 microstructure is characterized by a very fine dendritic/cellular structure, typically under 1 µm, with segregation (notably Nb and Mo) within interdendritic areas as well as high residual stresses. These features are provided by complex thermal cycle comprising fast heating to melt a specific area of the layer of powder and then rapid cooling and solidification (cooling rates around 10^6 K/s [1]). In addition, during the melting and solidification processes, the heat flux dissipation from the top of the samples to the building platform develops columnar grains which lead to anisotropic mechanical properties [14–21]. Consequently, the orientations of the components on the building platform must be carefully taken into account. For all these characteristics, it is therefore crucial to perform post heat treatments in order to reduce the residual stresses, to develop the desired microstructure and texture, and to achieve mechanical properties that are in line or exceed the post-heat treated IN625 alloy in the traditional state (e.g. heat-treated wrought IN625 alloy). For IN625 alloy, the heat treatments can be classified as stress relieving, recrystallization annealing as well as solution annealing. The first heat treatment aims to release the stresses within the material without significantly modifying the microstructure. The second type of heat treatment is designed to induce recrystallization with a reduced grain growth, for example, for applications that require high corrosion resistance while the third one promotes more remarkable recrystallization and grain growth in order to enhance the creep resistance [22].

Regarding the studies of the microstructure and texture of heat-treated LPBF IN625 by electron backscattered diffraction (EBSD), Fang et al. [23] revealed a strong reduction of the texture for heat treatments at 1150 °C. Li et al. [19] demonstrated that a standard annealing treatment at 980 °C for 1 hour promoted an initial recrystallization mechanism, reaching full recrystallization for thermal exposure at 1150 °C for 1 hour. Li et al. [18] reported the microstructure and texture of as-built and heat-treated IN625 samples reaching 1150 °C for 1 hour, also showing the effect of different heat treatments on the hardness and lattice parameters due to the precipitation.

The phase transformation plays a key role in determining the mechanical properties of as-built and heat-treated LPBF IN625 material. The alloy is subjected to the formation of the metastable γ" (Ni_3Nb – body-centered tetragonal), of its stable form δ (Ni_3Nb – orthorhombic), of Laves phases $(Ni, Cr, Fe)_2(Nb, Mo, Ti, Si)$ as well as of different types of carbides (e.g. MC, M_6C, $M_{23}C_6$). The γ" phases as well as fine and dispersed carbides enhanced the mechanical properties of the alloy while the δ, Laves phases and large carbides, especially along the grain boundaries (GBs), tend to be detrimental for its ductility and toughness [11,24–26]. For instance, in a previous work [17] some of the authors investigated the microstructure and mechanical properties of as-built, solution annealed (1150 °C for 2 hours), and different thermal exposure conditions (between 600 and 900 °C). It was shown that thermal exposures at 700 °C for 24 hours on the specimens in the as-built state resulted in an inhomogeneous distribution of γ" phases. It was attributed to the element segregations particularly Nb. Stoudt et al. [27] reported the accelerated kinetics of LPBF IN625 alloy under heat treatments, including the standard stress relieving at 870 °C for 1 hour, showing that the δ phase formation occurs in a shorter time with respect to the wrought IN625 alloy due to the segregation and very fine microstructure. Lindwall et al. [28] confirmed the accelerated phase transformation during heat-treatment of LPBF IN625 by means of thermodynamic simulation. Similarly, Zhan et al. [16] studied the microstructure of as-built and heat-treated IN625 at 870 °C for different times, revealing the formation of δ phase and MC carbides that can have a detrimental effect on the ductility of the alloy. All these studies clearly highlighted that the microstructure of heat-treated LPBF IN625 alloy must be carefully investigated in order to control the phases within LPBF material in heat-treated state.

Regarding the mechanical properties of post-processed LPBF IN625 alloy, Witkin et al. [29] highlighted that the hot isostatic pressing (HIP) process increased the fatigue resistance of LPFB IN625, even though the HIP treatment reduced the tensile strengths due to the coarsening of the microstructure. Gonzalez et

al. [30] compared the tensile properties of IN625 processed by LPBF, electron beam powder bed fusion and binder jetting technologies after HIP. They revealed that their tensile properties are in the range of the wrought IN625 alloy. Kreitcberg et al.[21,31] mainly focused their attention on the grain texture evolution of LPBF IN625 alloy under HIP treatment and different range of heat treatments, comparing the resulting tensile properties. However, they did not report the exact heat treatment conditions performed on the LPBF specimens.

Therefore, the current study provides a comprehensive investigation to correlate different microstructure characteristics with the tensile properties of LPBF IN625 in the as-built and heat-treated conditions. Employing X-ray diffraction (XRD), scanning electron microscopes (SEMs) equipped with Energy Dispersive X-ray spectrometry (EDS) and EBSD, a detailed description of the microstructure in regards to grain texture, GBs misorienation, present phases, and lattice parameter variation was provided. Finally, all these microstructural characteristics were correlated with the tensile properties of the heat-treated LPBF IN625 specimens built along two different orientations, showing the conditions to generate isotropic mechanical properties.

2.0 Materials and methods

2.1 Materials and LPBF process

The IN625 powder used in the current study was provided by EOS GmbH (Germany) with a manufacturer-certified chemical composition based on the UNS N06625. The chemical composition of the powder was evaluated by EDS analysis in order to provide a semi-quantitative analysis while the carbon content was determined using combustion infrared analysis by LECO - CS744 Series. The carbon content plays a crucial role in controlling the concentration and size of carbides during the solidification and heat treatments. The declared and analyzed chemical composition of the powder are reported in Table 1.

Powder particle size distribution is within the range with a d_{10} of 16 µm and d_{90} of 48 µm determined by laser granulometry diffraction with a Fritsch Analysette 22 Compact model.

Table 1 – 1) Chemical composition of IN625 powder declared by company in weight percentage (wt.%); 2) EDS analysis and combustion infrared analysis (for carbon) on the IN625 powder in wt.%.

	Ni	**Cr**	**Mo**	**Fe**	**Nb**	**Co**	**Si**	**Ti**	**Al**	**C**
1)	≥58.0	20-23	8-10	≤ 5	3.15-4.15	≤1.0	≤0.5	≤0.4	≤0.4	≤0.1
2)	66.1	19.3	8.6	0.6	4.1	0.1	0.4	0.4	0.4	0.012

An EOSINT M270 Dual Mode machine equipped with a 200 W Yb fiber laser was employed to fabricate the specimens. A set of cubic samples with a size of 15x15x15 mm^3 and cylindrical samples with length of 140 mm and a diameter of 15 mm were manufactured using a set of parameters determined in a previous work to obtain a relative density close to 100 % [14]. The applied process parameters were: scanning speed of 1200 mm/s, laser power of 195 W, hatching distance of 0.09 mm, a layer thickness of 0.02 mm and a scanning strategy involving a rotation of 67° of the laser among consecutive layers [14,17].

2.2 Material characterization techniques

The as-built and heat-treated cubic samples were used to analyze the microstructure while the as-built and heat-treated cylindrical bars were machined to obtain tensile specimens. The cylindrical bars were fabricated both along the building platform (xy plane) and normal to the building platform (z-axis) in order to determine the anisotropy in mechanical properties.

The microstructure investigations were performed in the middle of the cubic samples in order to avoid contamination with the building platform. The cubic samples were cut along the z-axis, polished up to 1 µm and then etched with Kalling's No.2 reagent. The etched samples along z-axis were analyzed by light optical microscope (LOM - Leica DMI 5000M) and scanning electron microscope (SEM - Phenom XL, Phenom-World BV, Eindhoven, The Netherlands) equipped with Energy Dispersive X-ray spectrometry (EDS). Moreover, higher magnification micrographs were obtained by FEG-SEM (Zeiss SupraTM40) while for the texture analysis, field emission gun scanning electron microscope (FEG-SEM, LEO 1550) equipped with an electron backscatter diffraction (EBSD) unit (Nordlys II detector - Oxford Instruments) were used. For texture analyses, the specimens were polished up to 0.04 µm by means of colloidal silica suspension analyzing the xy and zx planes. For the EBSD analysis, samples were tilted by 70° and scanned at 20 kV with a 1–2 µm step. For each condition, an area of 500x750 μm^2 was analyzed.

Additionally, it was evaluated the frequency of low angle grain boundaries (considered as LAGBs, $\theta \leq 10°$), high angle grain boundaries (considered as HAGBs $\theta > 10°$) as well as TGBs ($\theta = 60°$). TGBs ($\theta = 60°$) is based on the typical misorientation value for twinning grain boundary along (111) orientation [32].

The variation of the lattice parameter of the γ phase of as-built and heat-treated states was evaluated by X-ray diffraction (XRD, PANalytical, Almeno, The Netherland) using a CuKα radiation in a Bragg Brentano configuration from 30° to 100° with a step size of 0.013° and a counting time of 25 s per step. Considering the mechanical characterization, the tensile specimens comprised a gauge length of 40 mm, a reduced section of 51 mm and a diameter of 8 mm based on the ASTM E8M-09 were machined. Three specimens for each condition (three along the xy plane and three along the z-axis) were tested using an Zwick-Roell BT1 - FR100 machine applying a strain rate of 8.10^{-3} s^{-1} under the ASTM E8/E8M-09. Finally, the fracture surfaces of tensile samples were observed by SEM (SEM - Phenom XL, Phenom-World BV, Eindhoven, The Netherlands).

2.3 Heat treatments

The as-built IN625 alloy was subjected to the following heat treatments:

- A stress relieving treatment at 870 °C for 1 hour using a temperature typically recommended for IN625 alloy [33], defined in the following as HT1.
- An annealing treatment at 980 °C for 1 hour using a temperature typically recommended for IN625 alloy [33], defined as HT2.
- An annealing treatment at 1080 °C for 1 hour (using a temperature in the range of annealing treatment from 871 °C to 1092 °C) according to the ASTM B443, defined as HT3.
- A solution annealing treatment at 1150 °C for 2 hours, typically recommended for IN625 alloy [33], defined as HT4.

All the heat treatments were followed by water quenching (WQ) in order to inhibit the microstructure evolution during cooling [33].

3.0 Results and discussion

3.1 Microstructural evolution of LPBF IN625 alloy

The LPBF IN625 samples showed columnar grains in the as-built state (Fig. 1a) and in the heat-treated conditions HT1 and HT2 (Fig. 1b and 1c, respectively), along the building direction (z-axis). In contrast, the HT3 and HT4 (Fig.1d and 1e, respectively) revealed equiaxed grains with twin grain boundaries (TGBs). Moreover, it is interesting to note that the melt pool contours (MPCs) are clearly visible for the as-built and still visible for the HT1 state, while they disappear at higher thermal exposures. Some of the GBs, MPCs and TGBs are highlighted in the different conditions reported in Figure 1. This suggests that only heat treatments over 980 °C show indication of material homogenization.

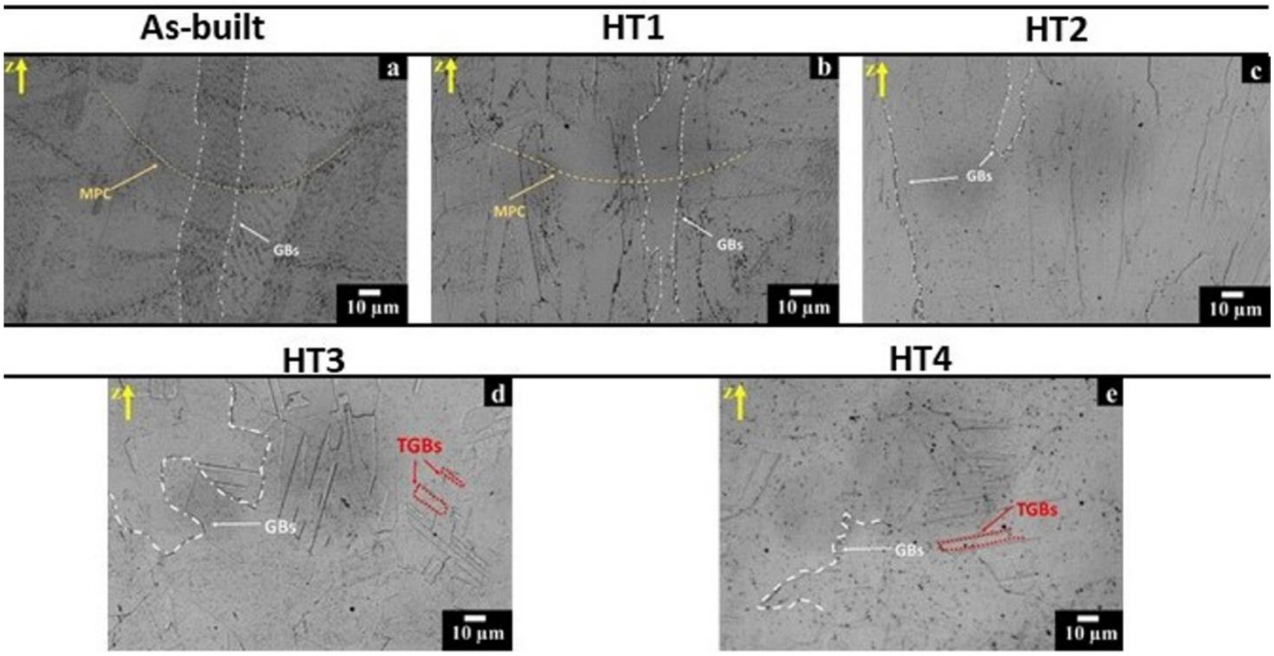

Figure 1 - LOM images of LPBF 625 samples along the building direction (z-axis): (a) as-built, (b) HT1, (c) HT2, (d) HT3 and (e) HT4. Kalling's No.2 reagent was used. Some melt pool contours (MPCs), grain boundaries (GBs), twin grain boundaries (TGBs) are indicated in the images.

3.1.1 As-built state

The microstructure of as-built LPBF IN625 samples has been widely investigated in the literature [14,17–21,31,34]. The melt pools consisted of a very fine dendritic and cellular structures (Fig. 2a) with a size typically less than 1 µm, as highlighted by the yellow arrows 1 and 2 in Figure 2b, respectively. In a previous study of some of the authors [17], TEM analysis revealed the formation of nanometric Nb-rich MC carbides formed by eutectic reaction during the solidification with a size less than 100 nm, pointed out by the precipitates with the bright contrast in FESEM images (Fig. 2c). Additionally, the same study

revealed segregation of Nb and Mo in the interdendritic regions. For Ni-based superalloys, Nb and Mo are characterized by a strong tendency to segregate within the interdendritic regions, highlighting the reason why the homogenization treatment is necessary [17,35].

During the investigation, no Laves phases were found within the material. This is consistent with the very low content of Fe within the starting powder (Table 1) hindering the precipiation of Laves phases. Additionally, low wt. % of Fe reduces the solidification range, limiting the amount of segregations [11]. A reduction of the solidification ranges can modify the grains size, thus affecting the mechanical properties. For instance, Khayat et al. [36] studied the effects of different level of Fe for IN625 processed by direct energy depostion. They revealed that low Fe concentration generates smaller grains, and therefore, higher tensile strenghts with respect to high Fe concentration.

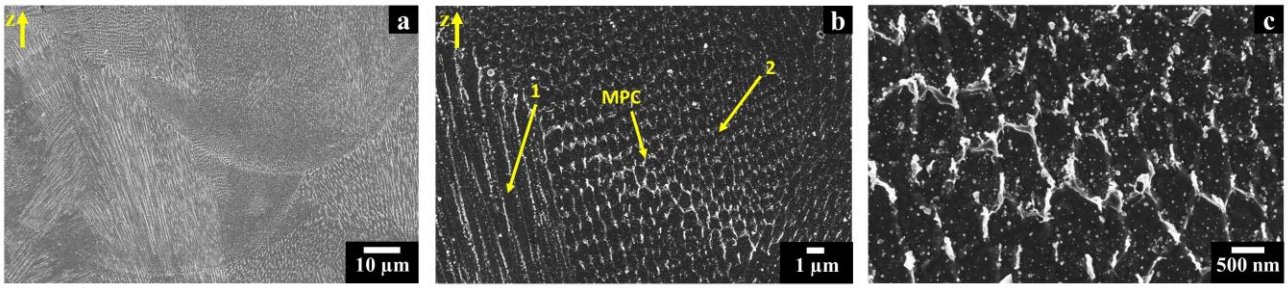

Figure 2 - FESEM images of the as-built LPBF IN625 samples along the building direction at different magnifications (a, b, c). Kalling's No.2 reagent was used. Columnar and cellular dendrites are indicated by yellow arrow 1 and 2, respectively.

3.1.2 HT1 condition

The SEM images in Figures 3 show the microstructure of the HT1 state. The sample exhibited very high concentration of δ phases located along the GBs, inter-dendritic areas as well as the MPCs, as highlighted in Figure 3a, 3b and 3c. The GBs and interdendritic areas tend to be decorated by the largest phases due to the enrichment in Nb segregation. The EDS analysis on the δ phases (Fig. 3d) revealed enrichment in Nb, depletion in Cr while there was no particular variation for the Ni. This is consistent with the δ phase which is composed of Ni and Nb [11,37]. The unaltered variation for Ni can be attributed to the very high concentration already present within the matrix, together with the small dimensions of the phase. High magnification view (Fig. 3c) also revealed the presence of spherical carbides, which could be primary carbides (the same as the as-built state) as well as new carbides generated by the thermal exposure.

The formation of δ phase and carbides, for LPBF IN625 alloy under stress relieving treatment at 870 °C found confirmation in the literature [16,27]. However, it is important to note that the size and concentration of these phases strongly depends on the heat treatment parameters such as temperature, time, cooling rates as well as the chemical composition of the alloy. In the current case, the small dimension of the carbides is mainly correlated to the very low carbon content and to fast cooling rates employed (water quenching) inhibiting their growth during the cooling. For the wrought IN625, the formation of δ phases should occur at longer thermal exposures, highlighting the greater kinetics phase formation for LPBF IN625 than traditional states [11,12]. This phenomenon derives from the segregation of Nb and Mo within the inter-dendritic areas which promote the formation of δ-phases under heat treatments [27,28]. According to the literature, these segregations can also help the formation of γ" phases extending the heating time at 8 hours [38]. For the alloy, this phenomenon may also be stimulated from high concentration of Ti and Al (within admitted range) since these elements tend to promote γ" phase formation under thermal exposures [11].

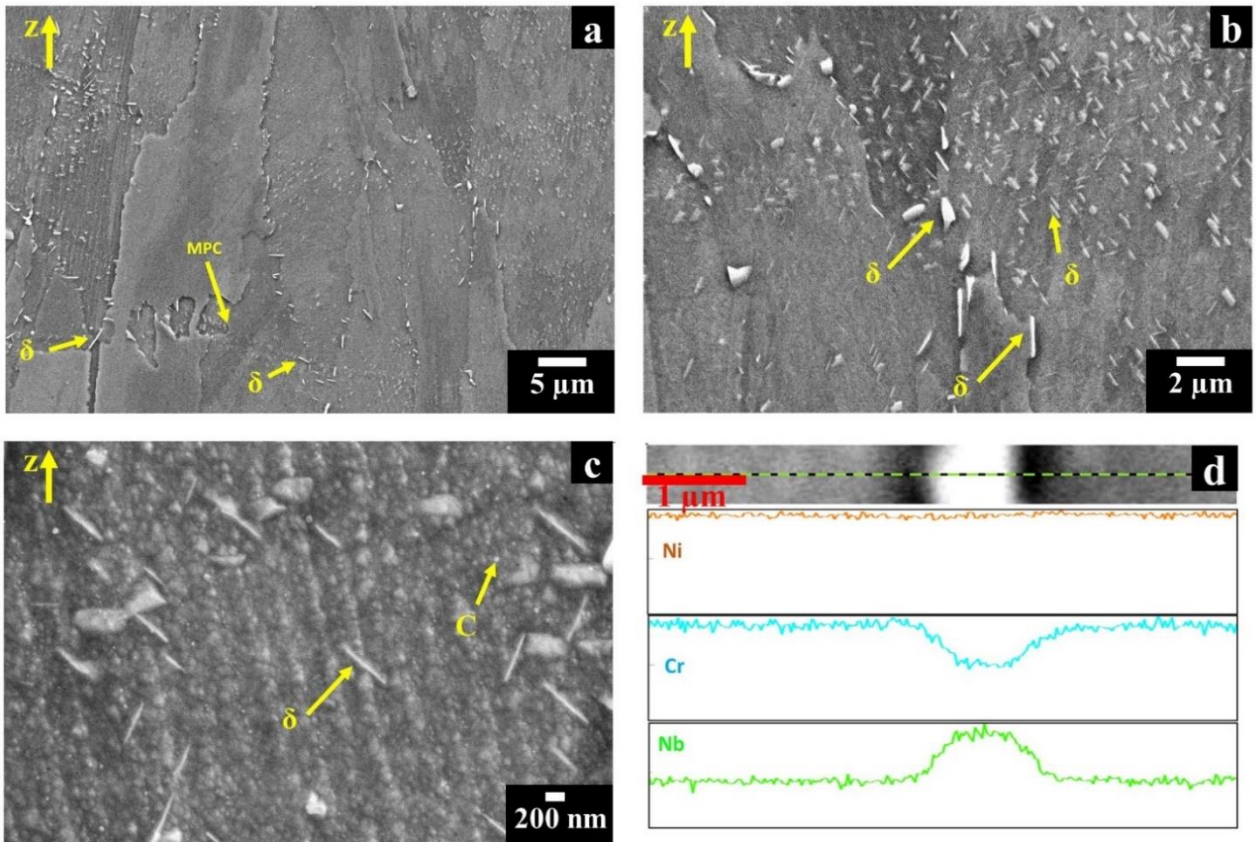

Figure 3 – FESEM images of HT1 state along the building direction at different magnifications. (a, b and c) showing the precipitates along the grains boundaries and within the grains, (d) EDS scan line on a δ phase. Kalling's No.2 etchant was used. The δ phases and carbides (abbreviated as C) are pointed out in the images.

3.1.3 HT2 condition

For wrought IN625 alloy, the annealing at 980 °C is a standard treatment [33]. Nevertheless, in the literature, there is a lack of extensive microstructural investigations of annealed LPBF IN625 samples in this condition.

Figure 4 reports the microstructure of LPBF IN625 in the HT2 condition. The microstructure exhibited columnar grains with the absence of the melt pool contours (Fig.4a). The largest precipitates were observed along the GBs (Fig 4b) while sub-micrometric carbides were mainly found close to the evanescent inter-dendritic areas, as pointed out by the yellow arrows in Fig.4c. EDS analysis on the largest precipitates (Fig. 4d) proved the enrichment in Nb and Mo coupled with the Ni and Cr depletion, thus suggesting the formation of carbides [11]. Considering the sub-micrometric carbides, it is therefore possible to infer that the inter-dendritic areas enriched in highly segregated elements promote their predominant formation in these areas.

The resulting microstructure of HT2 state consisted of γ phase with scattered carbides which are very similar to the wrought IN625 alloy annealed in the same condition, as indicated by the TTT diagram of the alloy [11,12].

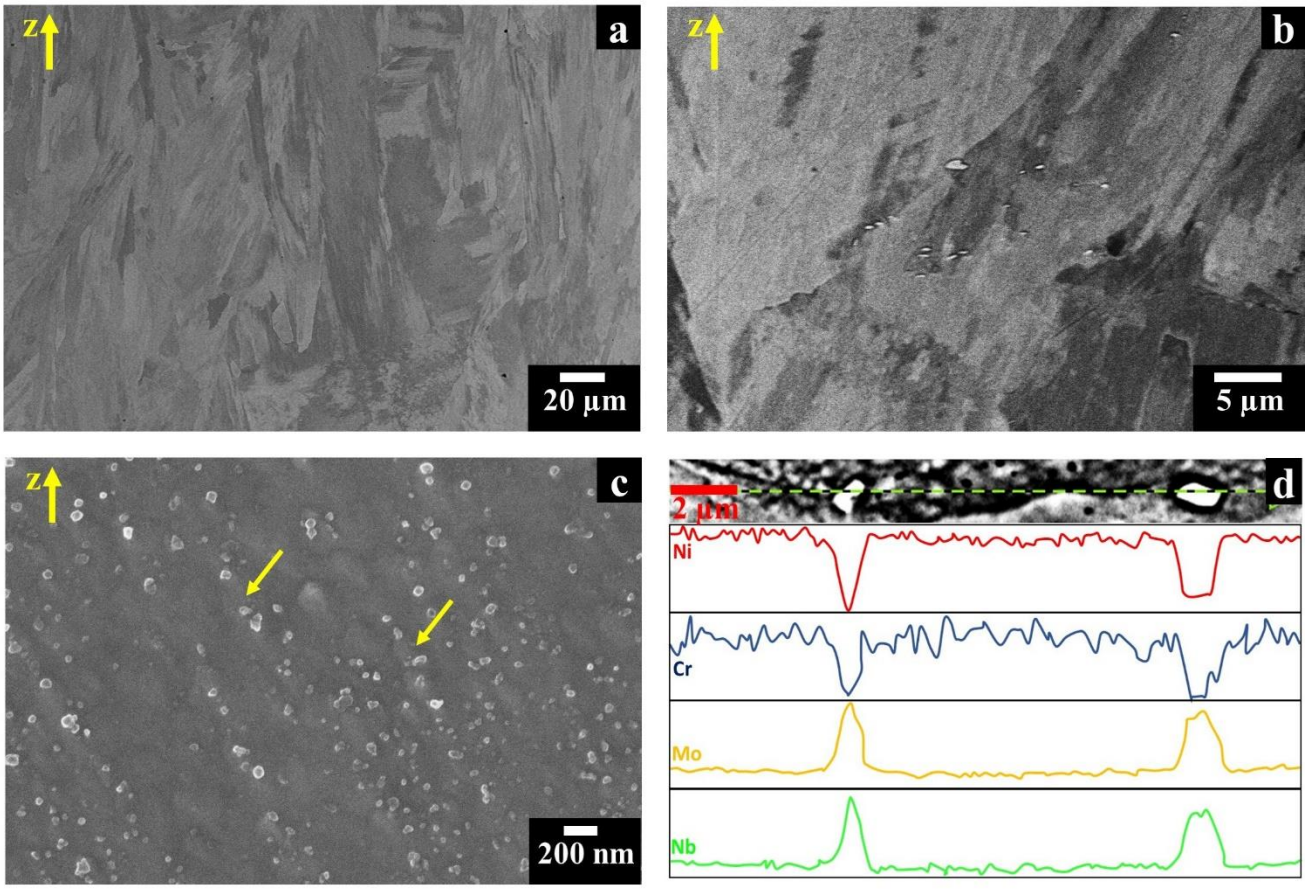

Figure 4- SEM images (a, b) and FESEM image (c) of HT2 state (along the building direction). (a,b) exhibiting the columnar grains, (b) showing the presence of intergranular carbides, (c) the almost invisible dendritic structures with orientated line of carbides as highlighted by yellow arrows, (d) EDS scan line on intergranular carbides showing enrichment n Nb and Mo together with depletion in Ni and Cr. Kalling's No.2 etchant was used.

3.1.4 HT3 and HT4 conditions

Figure 5 shows the microstructure of HT3 and HT4 states. The SEM images revealed equiaxed grains and TGBs, as observed in Fig. 5a and 5c. The microstructure of the two conditions seems quite similar with grains mainly from 5 to 70 µm for HT3 state and between 10 and 90 µm for HT4 condition. However, HT4 promoted a more significant homogenization which will be further discussed based on variation of the lattice parameters in the following paragraph. Figures 5b and 5d denote the presence of carbides derived from the growth of primarily formed MC carbides or formed during the thermal exposures. For both conditions, the size of the carbides is less than 1 µm. The limited size of the carbides can derive from the very low concentration of carbon within the powder and by the water quenching inhibiting the growth and formation of carbides during cooling.

In a previous investigation, the presence of MC carbides by TEM analysis on HT4 condition was shown [17]. Li et al. [19] reported that for solution annealed LPBF IN625 at 1150 °C for 1 hour, full recrystallization takes place with the formation of micrometric MC carbides. In this case, the larger carbides could be formed during the furnace cooling that provided the time for the growth of carbides in contrast to the water quenching, performed in the current work. On the other hand, Kreitcberg et al. [31] found the formation of M_6C carbides within the fully recrystallized LPBF IN625 alloy. The different type of carbides can be attributed to the different parameters for heat treatments such as time and temperature as well as difference in powder chemistry.

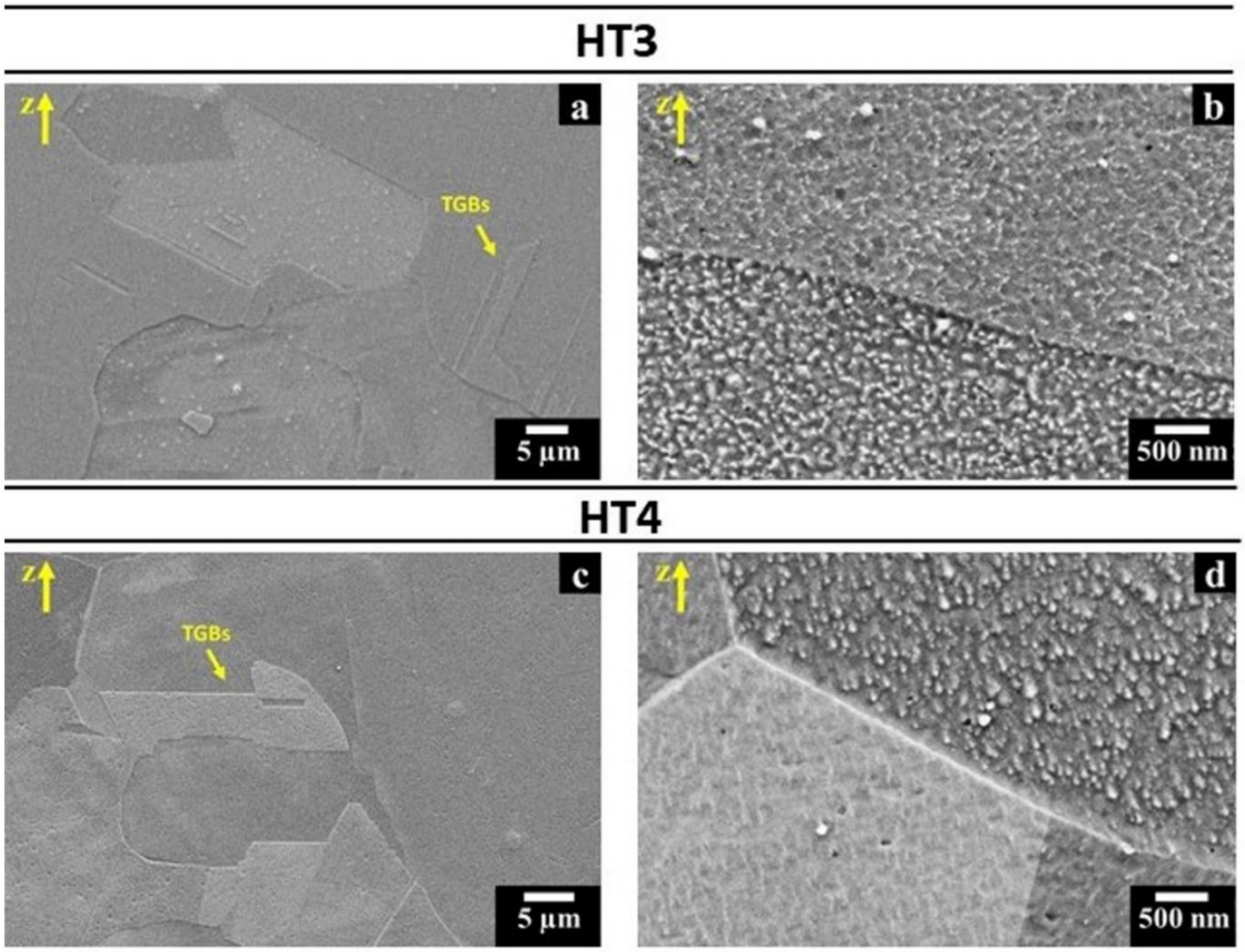

Figure 5 - FESEM images of the heat-treated IN625 samples: (a and b) HT3 state (c and d) HT4 state. Kalling's No.2 reagent was used.

3.2 XRD analysis

Figure 6 compares the lattice parameter of the γ phase for the as-built and heat-treated LPBF IN625 conditions in order to define the homogenization level. In fact, the homogenization has the scope to dissolve the segregation and inter-dendritic areas leading to increase the concentration of Nb and Mo within the matrix and thus broadening the lattice parameter of the γ phase. On the other hand, the precipitation of phases rich in Nb (as δ-phase, and carbides) reduces its concentration within the matrix causing a constriction of the lattice parameter [16,31]. For this study, the lattice parameter of the matrix was assessed using the Nelson-Riley extrapolations in order to limit the lattice parameter error [39,40].

HT1 state revealed an initial dissolution of the dendritic structures bringing Nb and Mo within the matrix and thus increasing the lattice parameter. In contrast, the formation of δ phases and carbides caused a depletion of elements as Nb. The sum of the two effects produced a slight increment of the lattice parameter with respect to the as-built condition. HT2 condition exhibited a more remarkable dissolution of the dendrites although carbides precipitation occurs, resulting in an increment in its lattice parameter. The HT3 state revealed a further increment of the lattice parameter, providing a partial microstructure homogenization. However, only HT4 condition exhibited a complete homogenization, as confirmed by the significant increment of the lattice parameter. In fact, the solution annealed LPBF IN625 material showed a lattice parameter compatible with the traditional solution annealed IN625 alloy (~ 3.609 Å) [41].

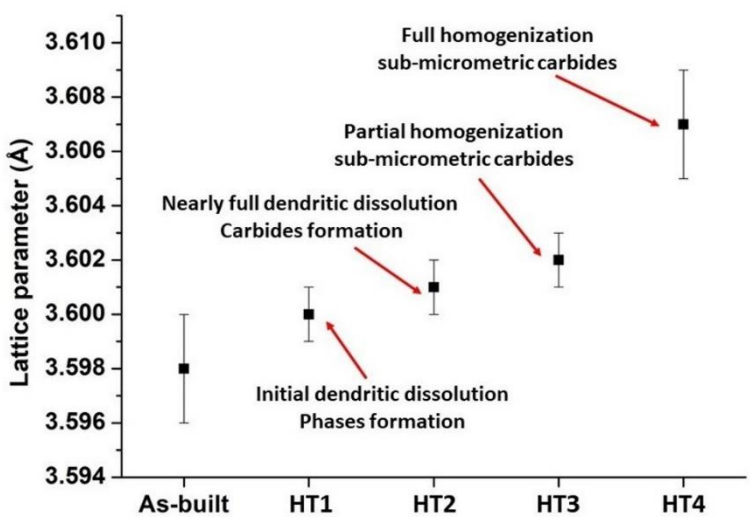

Figure 6- Lattice parameter variation of the γ matrix of the LPBF IN625 material under heat treatments.

3.3 Texture evolution under heat treatments

From the EBSD maps of as-built state (Fig. 7 a and f), a strong texture along the <001> direction (represented by the red color) is evident. This microstructural feature is common in Ni-based superalloys produced by LPBF during solidification [35 , 42]. The results show that the HT1 and HT2 have a neglectable effect on the texture of the LPBF IN625 materials (Fig. 7 b, g, c and h). On the other hand, heat treatment at higher temperatures HT3 (Fig. 7 d and i) and HT4 (Fig. 7 e and j) resulted in a random texture due to the formation of equiaxed grains.

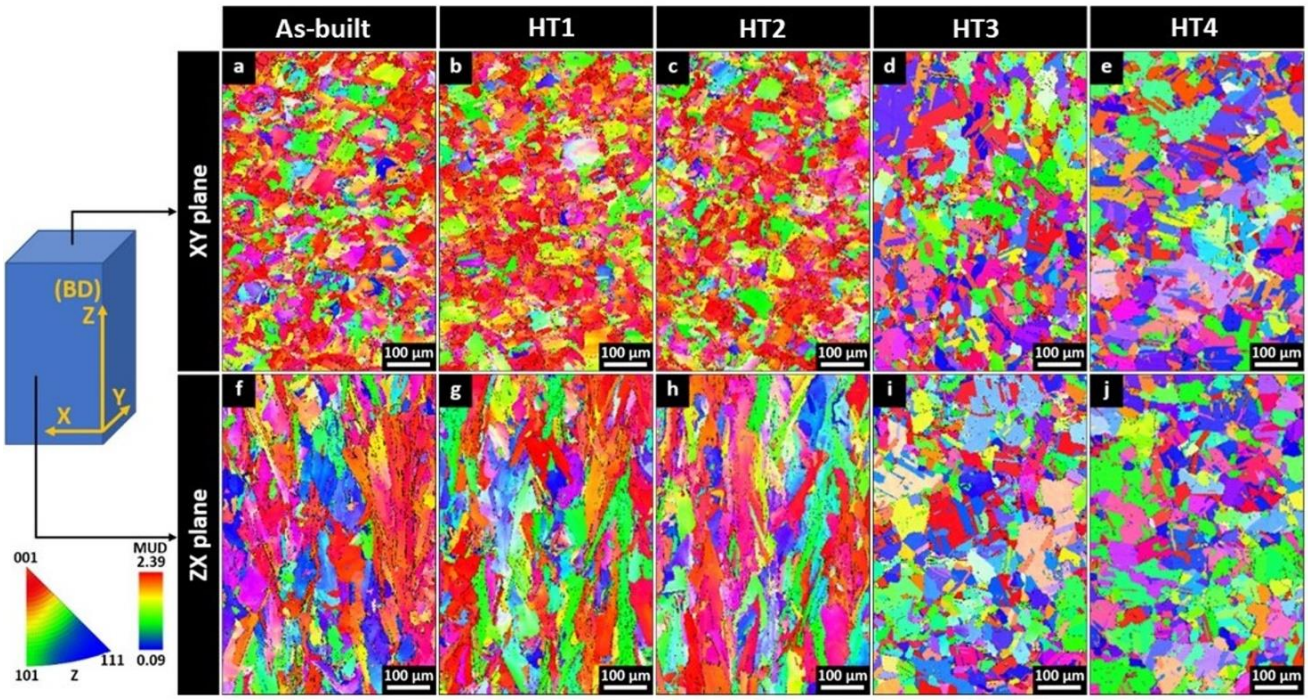

Figure 7 - EBSD maps (a-j) of the as-built, HT1, HT2, HT3 and HT4 conditions along the xy and zx planes. The position of the analyzed areas and the corresponding inverse pole figures are also reported.

Figures 8 shows the frequency and distribution of the grain boundary misorientations. The HAGBs θ >10° and LAGBs, θ≤10° are shown in black and white lines in the EBSD maps respectively (Fig. 8a-e). TGBs (θ = 60°) are highlighted in yellow (Fig. 8f and j). The graphic of the frequency of the grain misorientation distribution of the as-built and heat-treated conditions is also reported in Figure 8.

The as-built state (Fig. 8a and f) exhibited a very high fraction of LAGBs caused by the presence of substructures created by an array of dislocations due to the rapid solidification. The presence of LAGBs is reported in the literature on LPBF Ni-based superalloys [20,21,43]. These structures can hinder the movement of the dislocations explaining the high tensile strengths of the as-built state. The HT1 (Fig. 8b

and g) and HT2 (Fig. 8c and h) conditions showed a fraction of LAGBs similar to the as-built state. Additionally, it is interesting to note that thermal exposure at 980 °C resulted in the formation of a small amount of TGBs, indicating initial recrystallization. On the other hand, HT3 (Fig. 8d and i) and HT4 (Fig. 8e and j) conditions were subjected to more significant recrystallization reducing the LAGBs fraction to form HAGBs as well as TGBs. The plot of the frequency of LAGBs, HAGBs and TGBs is provided in Figure 8l.

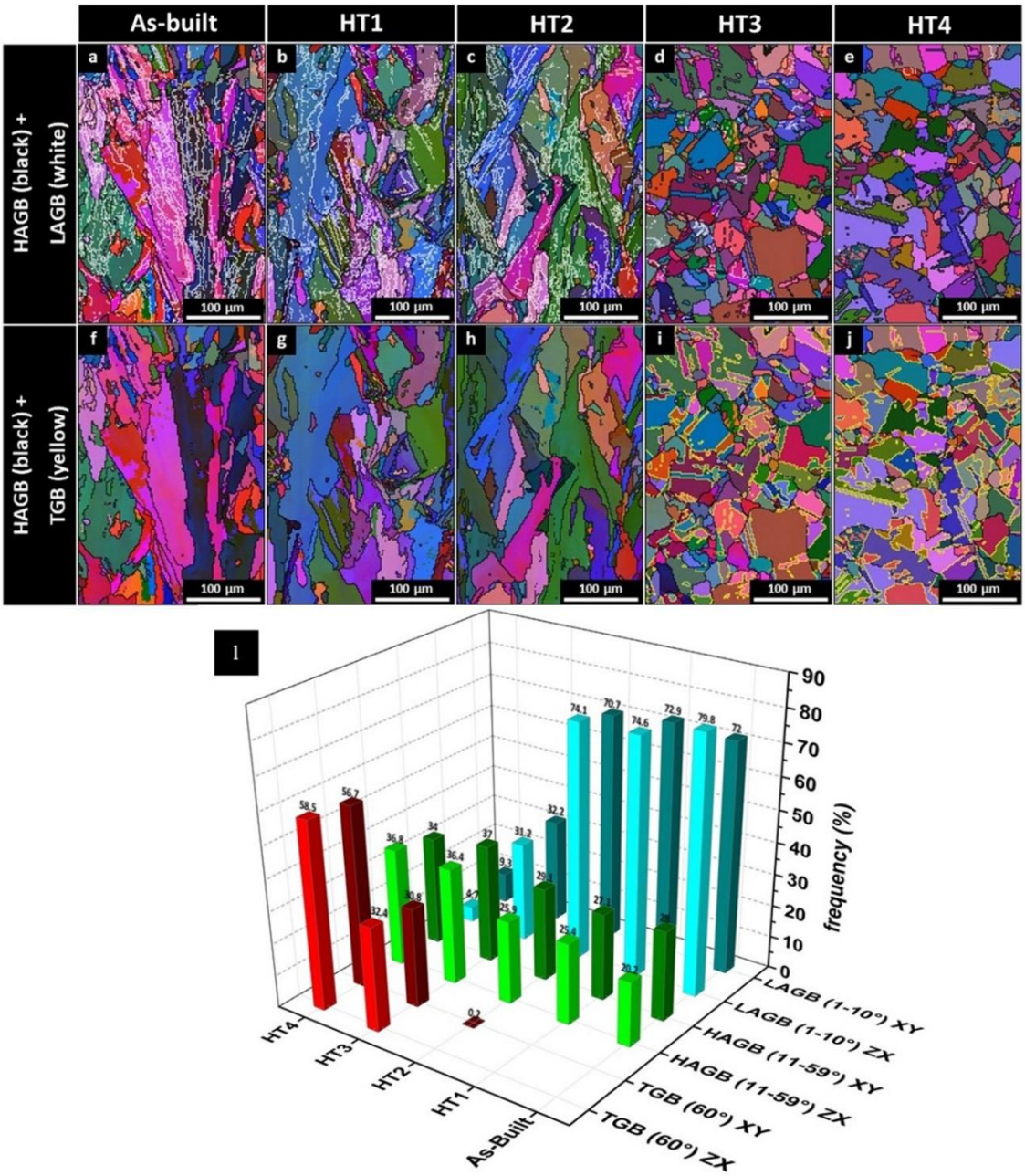

Figure 8 - EBSD images of the grain misorientation distribution of the as-built, HT1, HT2, HT3 and HT4 states along the building direction; (l) 3D column chart of the misorientation grain frequency of the LABG, HAGB and TGB for the different conditions along the two orientations.

3.4 Tensile properties

The tensile properties of as-built and heat-treated IN625 samples along the two different orientations are reported in Figure 9a and b. The as-built samples built along the xy plane revealed higher yield strength (YS) and ultimate tensile strength (UTS) together with lower ductility than as-built samples built along the z-axis. Similarly, this trend is still strongly observable for the HT1 and HT2 states. The anisotropy in mechanical properties of these conditions derives from the texture (as previously pointed out by the EBSD maps). However, for higher temperature treatments (HT3 and HT4), the mechanical property anisotropy was eliminated by the recrystallization mechanisms. The as-built and stress relieved specimens exhibited the highest YS and UTS and the lowest ductility compared to the other conditions (Fig. 9c). For the HT1 condition, the partial dissolution of the dendritic structures reduced the tensile strength while the formation of various precipitates enhanced the tensile strength. The combination of these two opposite effects generated a slight reduction of the tensile strengths for samples built along the xy plane while they were quite similar to as-built state for samples built along the z-axis. This could be attributed to different grain boundary strengthening along the two orientations due to the anisotropic microstructure.

The HT2 samples showed a reduction of tensile strengths correlated to an increment of the ductility with respect to the as-built and HT1 states. This derived from the almost full dissolution of dendritic structures. Finally, the HT3 and HT4 specimens revealed the highest ductility and the lowest tensile strengths (YS and UTS) with respect to the other states. This is caused by the recrystallization and grain growth involving the formation of equiaxed grains and the suppression of LAGBs with the increment of HAGBs and TGBs. Additionally, note that the TGBs form new crystal orientations which help to reduce the mechanical anisotropy along the different orientations.

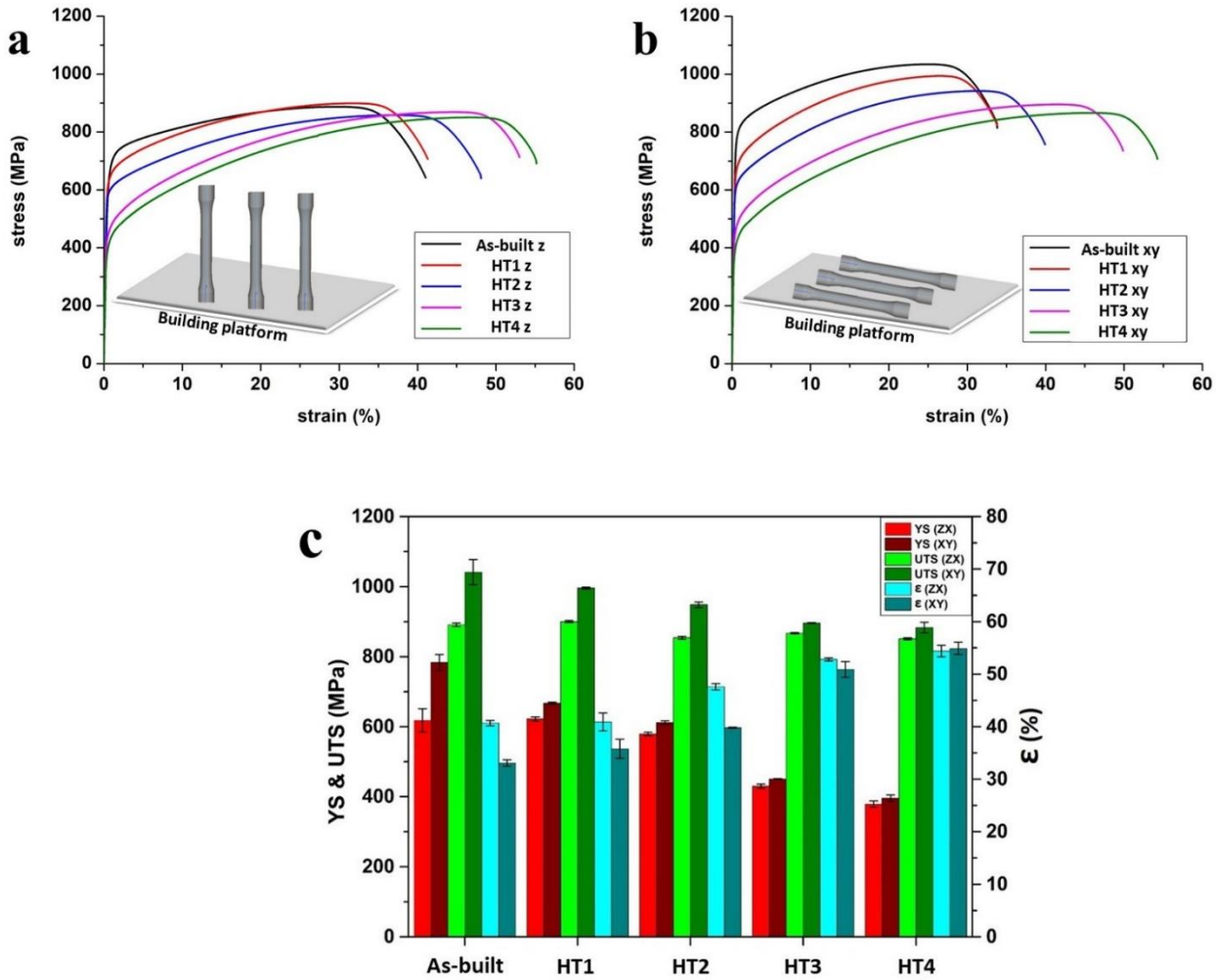

Figure 9 - Representative plots of tensile stress-strain diagrams of as-built and heat-treated specimens: (a) along the building direction (z-axis); (b) perpendicular to the building direction (xy plane); (c) Plots of the YS, UTS and ε recorded by LPBF IN625 tensile specimens in the as-built and heat-treated states along z-axis and xy plane.

The tensile properties of as-built LPBF IN625 state are in line with the value reported in the literature, taking into account that the mechanical properties are affected by several factors such as the type of LPBF machine used, the applied process parameters as well as the characteristic of the starting powder. Additionally, the as-built and HT1 samples exhibited values compatible with the as-rolled IN625 alloy. The values of tensile properties of annealed LPBF IN625 states (HT2 and HT3) and solution annealed state (HT4) exhibited values exceeding the minimum requirements for wrought IN625 in the annealed and solution annealed states based on ASTM B443. Finally, the HT4 samples revealed tensile properties compatible with LPBF IN625 subjected to HIP treatment performed at 1163 °C for 3 h and 102 MPa, applying a temperature slightly higher than our HT4 condition. This temperature triggers the formation

of equiaxed grains, generating a microstructure similar to the HT4 state [30]. The tensile properties of the investigated LPBF IN625 conditions, LPBF and wroughtIN625 states reported in the literature are given in Table 2.

Table 2 - Tensile properties of investigated LPBF IN625 states, LPBF IN625 and wrought IN625 alloys reported in the literature. The tensile properties are abbreviated as yield strength (YS), ultimate tensile strength (UTS) and elongation at break (ε).

Condition	YS (MPa)	UTS (MPa)	ε (%)
Previous study [17] *and current work*			
As-built z	618 ± 33	891 ± 5	40.7 ± 0.5
As-built xy [17]	783 ± 23	1041 ± 36	33.1 ± 0.6
HT1 z	621 ± 7	900 ± 2	40.9 ± 1.7
HT1 xy	667 ± 3	996 ± 3	35.8 ±1.8
HT2 z	579 ± 5	854 ± 4	47.6 ± 0.6
HT2 xy	612 ± 5	948 ± 8	39.8 ± 0.5
HT3 z	430 ± 6	867 ± 2	52.8 ± 0.3
HT3 xy	451 ± 1	896 ± 1	50.9 ± 1.5
HT4 z	379 ± 9	851 ± 3	54.5 ± 1.1
HT4 xy [17]	396 ± 9	883 ± 15	54.9 ± 1.2
Literature			
As-built xy [15]	641.5 ± 23.5	878.5 ± 1.5	30 ± 2
As-built z [44]	615 ± 50	900 ± 50	42 ± 5
As-built xy [44]	725 ± 50	990 ± 50	35 ± 5
As-rolled [13]	758-414	827-1103	60-30
Wrought IN625 grade 1*	>414	>827	>30
Wrought IN625 grade 2*	>276	>690	>30
As-built z+ HIP [30]	349 ± 5	842 ± 29	56 ± 6
As-built xy+ HIP [30]	396 ± 33	906 ± 28	62 ± 2

**According to ASTM B443 the minimum annealing temperature (grade 1 state) is 871 °C while the minimum solution annealing temperature (grade 2 state) is 1093 °C.*

The possibility of tailoring the mechanical properties increasing the ductility and reducing mechanical anisotropy can be crucial for the industry. The average YS and UTS vs the average ε are reported in Figure 10a and 10b. From the graphs, it is evident that the anisotropy must be carefully taken into account for the HT1 and HT2 states. These heat treatments could be applied to maintain high tensile strengths considering the level of ductility and mechanical anisotropy. On the other hand, the HT3 and HT4 states revealed isotropic mechanical properties and high ductility, indicating no relevant effects based on the building orientations.

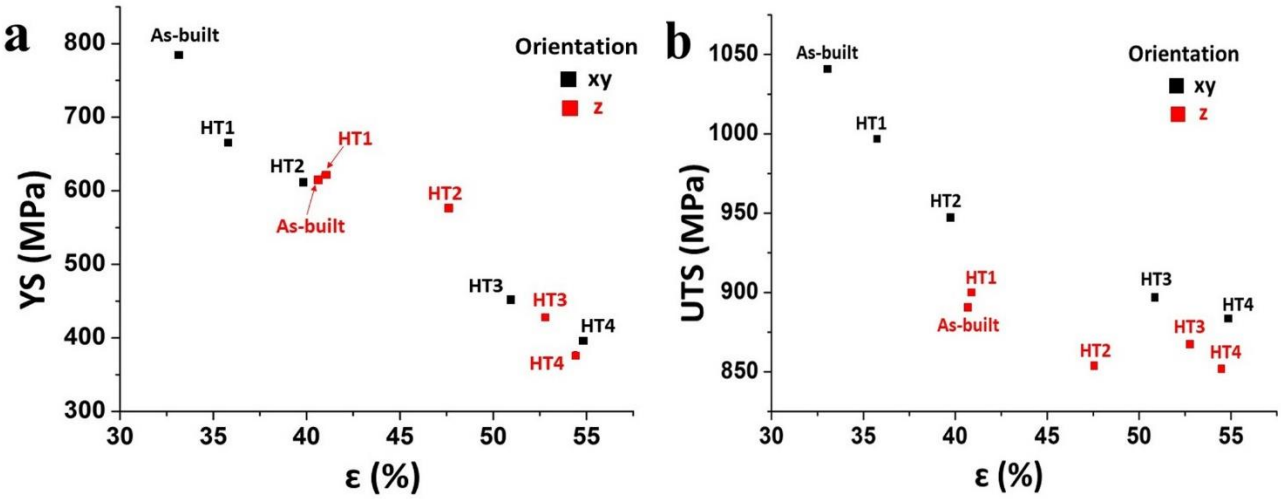

Figure 10- (a) Plot of the YS vs ε for the as-built and heat-treated conditions; (b) Plot of the UTS vs ε for the as-built and heat-treated conditions.

3.5 Fractography

Analyses of the fracture surface of specimens after tensile test were carried out on the as-built and heat-treated samples for components built along the z-axis. The as-built and HT1 states primarily showed a ductile fracture mode with the presence of fine dimples as well as few brittle fractures facets (Fig. 11a and 11b). These brittle areas may arise from the presence of segregated elements within the interdendritic areas as well as δ phase for the HT1 state. For the HT2 state (Fig.11c), the material revealed mostly ductile fracture with only rarely observed brittle facets with respect to the previous conditions. The brittle fracture may be provoked by the presence of intergranular carbides due to grain boundaries weakening. Contrary, the HT3 and HT4 states exhibited mainly a ductility fracture mode with large micro-voids generated by the coalescence of voids under the deformation during the tensile test, as can be seen in Figure 11d and 11e, respectively.

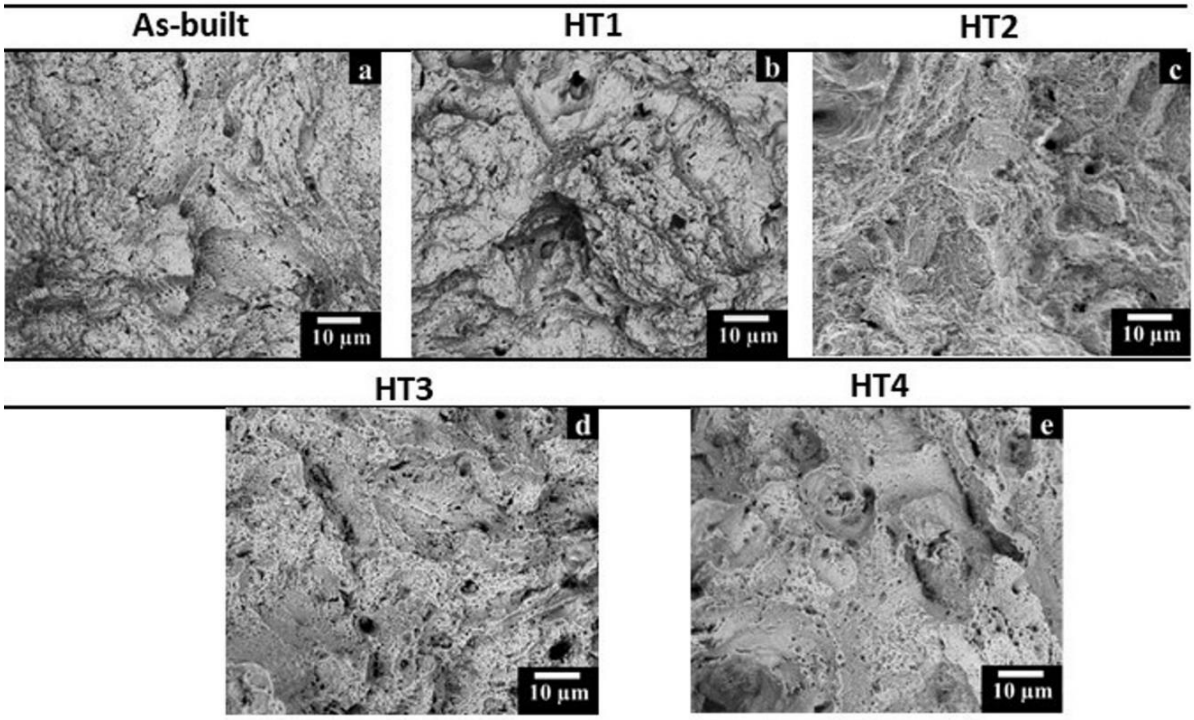

Figure 11 – SEM images showing the fracture surfaces of the (a) as-built state, (b) HT1, (c) HT2, (d) HT3 and (e) HT4. The images reported are related to the samples built along the z-axis.

4.0 Conclusions

The microstructure and tensile properties of the as-built, stress relieved (HT1), annealed (HT2 and HT3) as well as solution annealed (HT4) LPBF IN625 alloy were investigated. The microstructure and mechanical properties underwent several modifications under the current thermal exposures.

- The as-built LPBF IN625 sample exhibited columnar grains characterized by very fine dendritic/cellular structures with the presence of nanometric MC carbides and some segregation areas. The material had a strong texture along <001> direction with a high fraction of LAGBs. The combination of fine dendritic structures coupled to a high fraction of LAGBs tends to enhance the tensile strengths of the alloy.
- HT1 samples revealed the partial dissolution of dendritic structures with the formation of δ phase as well as possible fine carbides, showing an acceleration of the phases' formation with respect to the wrought condition due to the fine microstructure and segregation. The samples still showed the texture typical of the LPBF IN625 material with columnar grains and a very high fraction of LAGBs, revealing tensile properties not too different from the as-built state, especially for the samples built along z-axis.

- HT2 samples exhibited a more marked dendrite dissolution as well as the formation of micrometric carbides along the grain boundaries. Meanwhile, finer carbides can be detected within the grains, especially along the almost dissolved inter-dendritic areas. The EBSD maps still exhibited the texture with a high number of LAGBs, but start appearing very few TGBs, denoting initial recrystallization. The annealed state showed higher ductility correlated to lower tensile strengths with respect to the as-built and stress relieved states.
- HT3 and HT4 samples revealed the recrystallization and grain growth with the formation of equiaxed grains. The microstructure consisted of equiaxed grains and fine sub-micrometric carbides without exhibiting a trace of the dendritic structures. EBSD maps revealed the elimination of the texture with the drastic reduction of LAGBs coupled to the increment of HAGBs and TGBs. However, the complete homogenization is obtained only for the solution annealed samples (HT4) as confirmed by the lattice parameters determined by XRD analyses These microstructural modifications resulted in reduced YS and UTS and increased ductility with respect to the other conditions.
- Finally, it is interesting to note that the samples built along the xy plane revealed higher tensile strengths and lower ductility than samples built along the z-axis, essentially due to the texture. This behavior tends to disappear after the recrystallization induced by annealing at high temperature and solution annealing treatments (HT3 and HT4 conditions), indicating the elimination of the anisotropy in mechanical properties.

The current study highlighted the correlation between the microstructure and tensile properties of as-built, stress relieved, annealed and solution annealed LPBF IN625 materials, revealing that the tensile properties surpass the level settled for wrought heat-treated IN625 based on the ASTM B443. A similar result is a key factor to drive the application of post-heat treated LPBF IN625 alloy to different industrial fields.

Data availability

The authors declare that the main data supporting the findings of this work are available within the article and in Appendix A.

CRediT authorship contribution statement

Giulio Marchese: Conceptualization, Methodology, Investigation, Data curation, Writing - original draft, Writing - review & editing, Visualization. **Simone Parizia:** Methodology, Validation, Investigation, Data curation, Writing - original draft. **Masoud Rashidi:** Methodology, Investigation, Data curation, Writing - review & editing. **Abdollah Saboori:** Investigation, data curation, writing – review & editing. **Diego Manfredi**: Supervision, Writing - review & editing. **Daniele Ugues**: Supervision, Writing - review & editing. **Mariangela Lombardi:** Supervision, Writing – review & editing. **Eduard Hryha:** Writing - review & editing, Supervision, Funding acquisition. **Sara Biamino:** Conceptualization, Writing - review & editing, Supervision, Project administration, Funding acquisition.

Acknowledgement

Part of the work was performed in the framework of the PhD student exchange between Politecnico di Torino/CSFT@PoliTo and Centre for Additive Manufacturing – Metal (CAM^2), supported by Vinnova.

References

[1] M.M. Attallah, R. Jennings, X. Wang, L.N. Carter, Additive manufacturing of Ni-based superalloys: The outstanding issues, MRS Bull. 41 (2016) 758–764. doi:10.1557/mrs.2016.211.

[2] D.D. Gu, W. Meiners, K. Wissenbach, R. Poprawe, Laser additive manufacturing of metallic components: materials, processes and mechanisms, Int. Mater. Rev. 6608 (2012) 133–164. doi:10.1179/1743280411Y.0000000014.

[3] C.Y. Yap, C.K. Chua, Z.L. Dong, Z.H. Liu, D.Q. Zhang, L.E. Loh, S.L. Sing, Review of selective laser melting: Materials and applications, Appl. Phys. Rev. 2 (2015). doi:10.1063/1.4935926.

[4] D. Herzog, V. Seyda, E. Wycisk, C. Emmelmann, Additive manufacturing of metals, Acta Mater. 117 (2016) 371–392. doi:10.1016/j.actamat.2016.07.019.

[5] I.. Choudhury, M.. El-Baradie, Machinability of nickel-base super alloys: a general review, J. Mater. Process. Technol. 77 (1998) 278–284. doi:10.1016/S0924-0136(97)00429-9.

[6] E.O. Ezugwu, Key improvements in the machining of difficult-to-cut aerospace superalloys, Int. J. Mach. Tools Manuf. 45 (2005) 1353–1367. doi:10.1016/j.ijmachtools.2005.02.003.

[7] G. Marchese, G. Basile, E. Bassini, A. Aversa, M. Lombardi, D. Ugues, P. Fino, S. Biamino, Study of the microstructure and cracking mechanisms of Hastelloy X produced by laser powder bed fusion, Materials (Basel). 11 (2018). doi:10.3390/ma11010106.

[8] L.N. Carter, X. Wang, N. Read, R. Khan, M. Aristizabal, K. Essa, M.M. Attallah, Process

optimisation of selective laser melting using energy density model for nickel based superalloys, Mater. Sci. Technol. 0836 (2016) 1–5. doi:10.1179/1743284715Y.0000000108.

[9] G. Marchese, E. Bassini, A. Aversa, M. Lombardi, D. Ugues, P. Fino, S. Biamino, Microstructural Evolution of Post-Processed Hastelloy X Alloy Fabricated by Laser Powder Bed Fusion, Materials (Basel). 12 (2019). doi:10.3390/ma12030486.

[10] D. Tomus, P.A. Rometsch, M. Heilmaier, X. Wu, Effect of minor alloying elements on crack-formation characteristics of Hastelloy-X manufactured by selective laser melting, Addit. Manuf. 16 (2017) 65–72. doi:10.1016/j.addma.2017.05.006.

[11] S. Floreen, G.E. Fuchs, W.J. Yang, The Metallurgy of Alloy 625, Superalloys 718, 625, 706 Var. Deriv. Miner. Met. Mater. Socity. (1994) 13–37. doi:10.7449/1994/Superalloys_1994_13_37.

[12] L.E. Shoemaker, Alloys 625 and 725: Trends in properties and applications, 6th Int. Symp. Superalloys 718, 625, 706 Deriv. (2005) 409–418. doi:10.7449/2005/Superalloys_2005_409_418.

[13] special Metals, Inconel Alloy 625, (2006). http://www.specialmetals.com/assets/smc/documents/alloys/inconel/inconel-alloy-625.pdf (accessed April 28, 2018).

[14] G. Marchese, X. Garmendia Colera, F. Calignano, M. Lorusso, S. Biamino, P. Minetola, D. Manfredi, Characterization and Comparison of Inconel 625 Processed by Selective Laser Melting and Laser Metal Deposition, Adv. Eng. Mater. 19 (2017) 1–9. doi:10.1002/adem.201600635.

[15] P. Wang, B. Zhang, C.C. Tan, S. Raghavan, Y.F. Lim, C.N. Sun, J. Wei, D. Chi, Microstructural characteristics and mechanical properties of carbon nanotube reinforced Inconel 625 parts fabricated by selective laser melting, Mater. Des. 112 (2016) 290–299. doi:10.1016/j.matdes.2016.09.080.

[16] F. Zhang, L.E. Levine, A.J. Allen, M.R. Stoudt, G. Lindwall, E.A. Lass, M.E. Williams, Y. Idell, C.E. Campbell, Acta Materialia Effect of heat treatment on the microstructural evolution of a nickel- based superalloy additive-manufactured by laser powder bed fusion, 152 (2018) 200–214.

[17] G. Marchese, M. Lorusso, S. Parizia, E. Bassini, J.-W. Lee, F. Calignano, D. Manfredi, M. Terner, H.-U. Hong, D. Ugues, M. Lombardi, S. Biamino, Influence of heat treatments on microstructure evolution and mechanical properties of Inconel 625 processed by laser powder

bed fusion, Mater. Sci. Eng. A. 729 (2018) 64–75. doi:10.1016/j.msea.2018.05.044.

[18] S. Li, Q. Wei, Y. Shi, Z. Zhu, D. Zhang, Microstructure Characteristics of Inconel 625 Superalloy Manufactured by Selective Laser Melting, J. Mater. Sci. Technol. 31 (2015) 946–952. doi:10.1016/j.jmst.2014.09.020.

[19] C. Li, R. White, X.Y. Fang, M. Weaver, Y.B. Guo, Microstructure evolution characteristics of Inconel 625 alloy from selective laser melting to heat treatment, Mater. Sci. Eng. A. 705 (2017) 20–31. doi:10.1016/j.msea.2017.08.058.

[20] K.N. Amato, J. Hernandez, L.E. Murr, E. Martinez, S.M. Gaytan, P.W. Shindo, Comparison of Microstructures and Properties for a Ni-Base Superalloy (Alloy 625) Fabricated by Electron and Laser Beam Melting, J. Mater. Sci. Res. 1 (2012). doi:10.5539/jmsr.v1n2p3.

[21] A. Kreitcberg, V. Brailovski, S. Turenne, Effect of heat treatment and hot isostatic pressing on the microstructure and mechanical properties of Inconel 625 alloy processed by laser powder bed fusion, Mater. Sci. Eng. A. 689 (2017) 1–10. doi:10.1016/j.msea.2017.02.038.

[22] M.J. Donachie, S.J. Donachie, Superalloys: A technical Guide, second, ASM International, Materials Park, OH, 2002.

[23] X.Y. Fang, H.Q. Li, M. Wang, C. Li, Y.B. Guo, Characterization of texture and grain boundary character distributions of selective laser melted Inconel 625 alloy, Mater. Charact. (2018). doi:10.1016/j.matchar.2018.02.008.

[24] V. Shankar, K. Bhanu Sankara Rao, S.. Mannan, Microstructure and mechanical properties of Inconel 625 superalloy, J. Nucl. Mater. 288 (2001) 222–232. doi:10.1016/S0022-3115(00)00723-6.

[25] F. Cortial, J.M. Corrieu, C. Vernot-Loier, Influence of heat treatments on microstructure, mechanical properties, and corrosion resistance of weld alloy 625, Metall. Mater. Trans. A. 26 (1995) 1273–1286. doi:10.1007/BF02670621.

[26] J.F. Radavich, A. Fort, Effects of Long Time Exposure in Alloy 625 at 1200°F, 1400°F and 1600°F, Superalloys 718,625 Var. Deriv. (1994) 635–47.

[27] M.R. Stoudt, E.A. Lass, D.S. Ng, M.E. Williams, F. Zhang, C.E. Campbell, The Influence of Annealing Temperature and Time on the Formation of d -Phase in Additively- Manufactured Inconel 625, Metall. Mater. Trans. A. 49A (2018) 3028–3037. doi:10.1007/s11661-018-4643-y.

[28] G. Lindwall, C.E. Campbell, E.A. Lass, F. Zhang, M.R. Stoudt, Simulation of TTT Curves for Additively Manufactured Inconel 625, Metall. Mater. Trans. A. 50 (2019) 457–467. doi:10.1007/s11661-018-4959-7.

[29] D.B. Witkin, P. Adams, T. Albright, Microstructural evolution and mechanical behavior of nickel-based superalloy 625 made by selective laser melting, 9353 (2015) 93530B. doi:10.1117/12.2083699.

[30] J.A. Gonzalez, J. Mireles, S.W. Stafford, M.A. Perez, C.A. Terrazas, R.B. Wicker, Characterization of Inconel 625 Fabricated Using Powder-Bed-Based Additive Manufacturing Technologies, J. Mater. Process. Tech. 264 (2018) 200–210. doi:10.1016/j.jmatprotec.2018.08.031.

[31] A. Kreitcberg, V. Brailovski, S. Turenne, Elevated temperature mechanical behavior of IN625 alloy processed by laser powder-bed fusion, Mater. Sci. Eng. A. 700 (2017) 540–553. doi:10.1016/j.msea.2017.06.045.

[32] C. Blochwitz, W. Tirschler, Twin boundaries as crack nucleation sites, 41 (2005) 32–41. doi:10.1002/crat.200410305.

[33] H. Chandler, ed., Heat Treater' s Guide: Practices and Procedures for Nonferrous Alloys, ASM International, Materials Park, OH, 1996.

[34] G. Marchese, L. Massimo, C. Flaviana, E.P. Ambrosio, M. Diego, P. Matteo, B. Sara, U. Daniele, F. Paolo, Microstructural Investigation of Heat Treated Inconel 625 Fabricated Through Direct Metal Laser Sintering, in: EPMA (Ed.), World Powder Metall. 2016, Hamburg (DE), 2016: pp. 1–6.

[35] E. Chlebus, K. Gruber, B. Kuźnicka, J. Kurzac, T. Kurzynowski, Effect of heat treatment on the microstructure and mechanical properties of Inconel 718 processed by selective laser melting, Mater. Sci. Eng. A. 639 (2015) 647–655. doi:10.1016/j.msea.2015.05.035.

[36] Z.R. Khayat, T.A. Palmer, Impact of iron composition on the properties of an additively manufactured solid solution strengthened nickel base alloy, Mater. Sci. Eng. A. 718 (2018) 123–134. doi:10.1016/j.msea.2018.01.112.

[37] F.J. Xu, Y.H. Lv, B.S. Xu, Y.X. Liu, F.Y. Shu, P. He, Effect of deposition strategy on the microstructure and mechanical properties of Inconel 625 superalloy fabricated by pulsed plasma arc deposition, Mater. Des. 45 (2013) 446–455. doi:10.1016/j.matdes.2012.07.013.

[38] E.A. Lass, M.R. Stoudt, M.B. Katz, M.E. Williams, Precipitation and dissolution of δ and γ″ during heat treatment of a laser powder-bed fusion produced Ni-based superalloy, Scr. Mater. 154 (2018) 83–86. doi:10.1016/j.scriptamat.2018.05.025.

[39] B. Fultz, J. Howe, Diffraction and the X-Ray Powder Diffractometer, in: Transm. Electron Microsc. Diffractometry Mater., Springer Berlin Heidelberg, Berlin, Heidelberg, 2013: pp. 1–57.

doi:10.1007/978-3-642-29761-8_1.

[40] J.B. Nelson, D.P. Riley, An experimental investigation of extrapolation methods in the derivation of accurate unit-cell dimensions of crystals, Proc. Phys. Soc. 57 (1945).

[41] S.K. Rai, A. Kumar, V. Shankar, T. Jayakumar, K.B.S. Rao, B. Raj, Characterization of microstructures in Inconel 625 using X-ray diffraction peak broadening and lattice parameter measurements, Scr. Mater. 51 (2004) 59–63. doi:10.1016/j.scriptamat.2004.03.017.

[42] L.N. Carter, C. Martin, P.J. Withers, M.M. Attallah, The influence of the laser scan strategy on grain structure and cracking behaviour in SLM powder-bed fabricated nickel superalloy, J. Alloys Compd. 615 (2014) 338–347. doi:10.1016/j.jallcom.2014.06.172.

[43] P. Kanagarajah, F. Brenne, T. Niendorf, H.J. Maier, Inconel 939 processed by selective laser melting: Effect of microstructure and temperature on the mechanical properties under static and cyclic loading, Mater. Sci. Eng. A. 588 (2013) 188–195. doi:10.1016/j.msea.2013.09.025.

[44] EOS, EOS GmbH - Electro Optical Systems, Material data sheet - EOS Nickel Alloy IN625, (2011) 1–5. https://www.eos.info/material-m (accessed March 27, 2019).